Science and Technology of Advanced Materials

ISSN: (Print) (Online) Journal homepage: www.tandfonline.com/journals/tsta20

Durable superhydrophobic surfaces on 3D-Printed structures inspired by beehive architecture

Kengo Manabe, Makoto Saikawa, Tetsuhiro Iwai & Yasuo Norikane

To cite this article: Kengo Manabe, Makoto Saikawa, Tetsuhiro Iwai & Yasuo Norikane (24 Mar 2025): Durable superhydrophobic surfaces on 3D-Printed structures inspired by beehive architecture, Science and Technology of Advanced Materials, DOI: 10.1080/14686996.2025.2481824

To link to this article: https://doi.org/10.1080/14686996.2025.2481824

Publisher: Taylor & Francis & The Author(s). Published by National Institute for Materials Science in partnership with Taylor & Francis Group.

Journal: *Science and Technology of Advanced Materials*

DOI: 10.1080/14686996.2025.2481824

Durable Superhydrophobic Surfaces on 3D-Printed Structures Inspired by Beehive Architecture

Kengo Manabe,[*,†] *Makoto Saikawa,*[†,‡] *Tetsuhiro Iwai,*[†] *and Yasuo Norikane*[†,§]

[†]National Institute of Advanced Industrial Science and Technology (AIST), Higashi 1-1-1, Tsukuba, Ibaraki, 305-8565, Japan

[‡]Graduate School of Science and Technology, University of Tsukuba, Tsukuba, Ibaraki, 305-8571, Japan

[§] Faculty of Pure and Applied Sciences, University of Tsukuba, Tsukuba, Ibaraki, 305-8571, Japan

Corresponding author: kengo.manabe@aist.go.jp*

ABSTRACT

This study presents an approach for fabricating durable superhydrophobic surfaces on 3D-printed structures inspired by the architectural design of beehives. Using fused deposition modeling (FDM) 3D printing technology, hexagonal macrostructures were fabricated using polylactic acid (PLA) filament. These structures were designed to protect an inner layer of hydrophobic nanoparticles, which were deposited by a squeegee coating method and immobilized by a photocurable resin. The relationship between hexagonal area size (ranging from 24 to 200 mm^2) and the durability of superhydrophobic properties under frictional stress was systematically investigated. Wettability and surface morphology analyses performed before and after the friction tests showed that structures with hexagonal areas between 40 and 80 mm^2 retained superhydrophobicity even after 100 friction cycles, while larger hexagonal configurations exhibited diminished performance. To elucidate the underlying mechanisms, a theoretical model based on the Cassie-Baxter equation was developed and compared with experimental values alongside surface observations. This research advances the development of durable and functional superhydrophobic surfaces in 3D-printed materials, with promising implications for industries requiring water-repellent and self-cleaning technologies.

KEYWORDS

3D print, wettability, superhydrophobicity, biomimetics, surface structures

1. Introduction

Achieving a carbon-neutral society necessitates materials science and manufacturing breakthroughs guided by circular economy principles. Among emerging innovations, 3D printing (additive manufacturing) is revolutionizing production by enabling the direct fabrication of intricate geometries through digital design and layer-by-layer material deposition [1]. Compared to conventional techniques such as injection molding and machining, 3D printing offers key advantages, including reduced material waste, enhanced customization, greater design flexibility, and material reutilization [2-4]. These attributes establish 3D printing as a pivotal technology in sustainable manufacturing and remanufacturing, with industrial adoption expected to accelerate [5].

Despite these advancements, the surface properties of 3D-printed products remain a critical yet underexplored aspect. In fields such as architecture and automotive manufacturing, surface finish has a significant impact on product aesthetics, functionality, and durability [6,7]. Protective coatings are often required to mitigate environmental degradation, prevent corrosion, and enhance mechanical resilience. Among these, superhydrophobic coatings—characterized by extreme water repellency— are particularly promising due to their self-cleaning and anti-fouling properties [8].

Superhydrophobicity, inspired by natural surfaces such as lotus leaves, is defined by a water contact angle greater than 150° [9-12]. This property extends beyond mere hydrophobicity, and confers benefits such as surface dryness and resistance to fouling, making it ideal for 3D printing applications [13-16]. Achieving superhydrophobicity requires a combination of low surface energy—typically achieved through chemical modification—and micro/nanoscale surface texturing to minimize solid-liquid contact [17,18]. However,

these intricate structures are highly susceptible to mechanical degradation, with even minor abrasion compromising their functionality by disrupting the surface topography [19,20].

Various strategies have been proposed to address this challenge [21], including enhancing adhesion layers [22,23], integrating sacrificial structures [24,25], and developing hierarchical self-similar textures [26,27]. In 3D printing, efforts have focused on the fabrication of hierarchical structures essential for superhydrophobicity and the post-processing modification of surfaces [16,28-31]. As some typical examples of superhydrophobic structures using 3D printing, Barraza et al. [16] achieved superhydrophobicity with a high water contact angle of 165° and low contact angle hysteresis by forming a simple mountain-shaped stripe structure using stereolithographic (SLA) 3D printing and coating it with hydrophobic TiO_2 nanoparticles. Wu et al. [28] developed a multilayered superhydrophobic structure by integrating hydrophobic silica nanoparticles with a sintered polymer microparticle network using selective laser sintering (SLS) 3D printing. Notably, even after surface abrasion, the underlying layers exhibited hydrophobic properties similar to the outermost surface. An example of superhydrophobic structures fabricated using polylactic acid (PLA) and Fused Deposition Modeling (FDM) 3D printing is the work of Amin et al. [29], who fabricated a pyramid-patterned textured surface. Their study provided a detailed analysis of the influence of surface feature spacing on the wetting mechanism. As summarized in Table S1, which compiles various studies on 3D-printed superhydrophobic structures, SLA and SLS techniques have been predominantly employed. The primary research focus has been on enhancing durability by exploiting hierarchical, self-similar textures that maintain their surface properties even after mechanical wear or cutting. However, coatings applied by painting or thin layer deposition remain vulnerable to mechanical wear, and hierarchical self-similar textures can also lead to surface deformation, degradation of low-surface-energy materials, and subsequent loss of both aesthetics and

functionality. Consequently, superhydrophobicity and mechanical robustness are often considered mutually exclusive, highlighting the need for further research to bridge this gap in both fundamental understanding and practical implementation. This issue is particularly pertinent for 3D-printed products, which may be subjected to various mechanical stresses throughout their lifecycle.

This study aims to develop highly durable superhydrophobic surfaces for 3D-printed materials and to systematically investigate their friction and wear resistance. Inspired by drone beehives—specifically the wax-capped inner honeycomb structure (Figure 1a) [32,33]—we propose a three-layer architecture: (1) a nanostructured layer to impart superhydrophobicity, (2) a macrostructured outer shell with internal convex elements for mechanical durability, and (3) an intermediate layer to ensure strong adhesion. The macrostructure composed of polylactic acid (PLA), a leading biodegradable bioplastic [34-36], is fabricated using commercially available 3D printing technology and serves to shield the hydrophobic nanostructure. A photocurable resin at the interface enhances adhesion, while internal convex spikes counteract resin concavity induced by surface tension. This design preserves superhydrophobic properties, including anti-fouling and self-cleaning functions, even in harsh environments, while enabling cost-effective and scalable manufacturing. The proposed approach has the potential to broaden the applicability of superhydrophobic coatings across various industries, contributing to the development of more durable and functional 3D-printed products.

2. Experimental

2.1. Materials

For the 3D printing process, poly-lactic acid (PLA) filament (Raise3D standard PLA filament, diameter: 1.75 mm, JAPAN 3D PRINTER Co., Ltd., Tokyo, Japan) was used to construct the macrostructures. The superhydrophobic nanostructures were constructed using hydrophobic fumed silica nanoparticles (7 nm diameter, AEROSIL RX300, NIPPON AEROSIL CO., LTD., Tokyo, Japan) dispersed in acetone (Kanto Chemical Co. Inc., Tokyo, Japan). A water-washable high-toughness acrylic resin (SK honpo, FELIDENTIA CAPITAL LIMITED, Tokyo, Japan) was used as a photocurable resin to bond the macrostructures and nanostructures.

2.2. 3D printed macrostructures

The design of the 3D-printed macrostructures was inspired by the honeycomb structure of drone beehives, which represents a biomimetic durable structure. The outermost surface was designed with a hexagonal geometry arranged in the densest possible configuration to maximize exposure of the embedded hydrophobic nanoparticles. The size constraints of this arrangement were dictated by the resolution limits of the 3D printer. The macrostructures were designed using Fusion360 (Autodesk, Inc., CA, US), a 3D CAD program. The CAD data was exported in STL format and then converted to GCode for 3D printing. The design values for the common structure in this study were a height of 5 mm for the entire structure and a height of 4 mm for the bridge and spikes (i.e., the depth of the concavity inside the hexagon). A Raise3D Pro3 fused deposition modeling (FDM) printer was used to fabricate the models using PLA filament. The 3D printer was equipped with a steel nozzle with a 0.4

mm diameter orifice. Key printing parameters included: nozzle temperature of 210°C, build plate temperature of 60°C, layer height of 0.1 mm, and print speed of 60 mm/s. The parameter settings were adjusted based on the 3D printer manufacturer's recommended values. It is desirable to make adjustments as necessary depending on the surrounding environment during 3D printing and the condition of the filament. To maintain filament quality and prevent moisture-induced degradation, the PLA filament was dried at 50°C for 8 hours after use and stored in a sealed bag with silica gel desiccant.

2.3. Superhydrophobic treatment

To impart superhydrophobicity, hydrophobic fumed silica nanoparticles and photocurable resin were applied to the 3D printed structures. The nanoparticles were dispersed in acetone at a concentration of 2 wt.%. The treatment process involved multiple steps of coating and UV curing. First, uncured photocurable resin was filled into the structure using a glass rod squeegee technique, followed by the squeegee coating of the nanoparticle solution. The uncured excess resin that overflowed from the structure was removed through squeegee coating. The coating was partially cured with 30 seconds of UV irradiation, followed by another layer of nanoparticle solution. This was followed by 60 seconds of UV irradiation for further curing. A final layer of nanoparticle solution was squeegeed and the coating was fully cured with 10 minutes of UV exposure. Repeated layer-by-layer application of nanoparticles allows for embedding of nanoparticles into the resin surface and uniform distribution of nanoparticles on the surface. The concave part of the structure was filled with the resin-nanoparticle composite, and the composite was 4 mm thick. The complete process is shown in Figure 1b.

2.4. Characterization

The surface morphology was analyzed using a stereomicroscope (WILD MZ8, Leica Camera Japan Co., Ltd., Tokyo, Japan) equipped with a digital microscope camera (HAYEAR 4K UHD HY-6110, Shenzhen Hayear Electronics Co. Ltd., Shenzhen, China). A 3D scanning laser microscope (VK-X150, KEYENCE Corp., Osaka, Japan) was used for detailed evaluation of the surface condition of the pre- and post-friction tests. The wetting behavior of the surfaces was evaluated using a contact angle meter (Drop Master 300K, Kyowa Interface Science Co., Ltd, Saitama, Japan) with water droplets of 5 μL volume. Durability tests for superhydrophobicity involved linear reciprocating friction tests under a load of 100 g (7 mN/mm^2), performed at a speed of 20 mm/s for 100-2000 cycles. The friction counterpart material consisted of microfiber polyester cloth (~1 mm thick) with a contact area of approximately Φ15.3 mm.

3. Results and Discussion

3.1. 3D printed structures and surface design

This study focused on the development of a biomimetic structure inspired by the natural architecture of beehives, using a densely packed hexagonal pattern designed with 3D CAD software (Figure 2). Hexagonal structures of varying areas (24, 40, 80, 120, 160, and 200 mm^2) were fabricated to investigate the relationship between structural dimensions and frictional durability. The design included bridges (convex features connecting the hexagonal voids) and spikes (protrusions within each hexagon corresponding to the height of the bridges). These spikes were included to counteract surface tension effects and resin curing

induced concavity in larger hexagons. The initial specifications defined a bridge width of 0.2 mm and a spike tip radius of 0 mm. Detailed design parameters are shown in Table S1, with the corresponding 3D CAD model shown in the first column of Figure 2.

After fabrication using Fused Deposition Modeling (FDM) 3D printing, deviations from the original design were observed under a stereomicroscope. As expected with FDM technology, which relies on thermal melting of the filament, deviations were noted primarily in the bridge regions [37]. Actual bridge widths ranged from 0.23 to 0.33 mm, representing a 10-50% increase over the intended dimensions. This increase resulted in slightly shorter bridge lengths. In addition, the tips of the spikes, originally designed as sharp points, appeared rounded with radii ranging from 0.46 to 0.87 mm. The larger hexagonal structures conformed more closely to their design specifications, suggesting that commercial low-cost FDM printers are more effective at producing larger geometries. However, structures fabricated under the smallest condition (24 mm^2) encountered significant challenges; over half of the internal spikes were improperly formed due to PLA filament pulling or tip deformation during printing.

After 3D printing, a superhydrophobic treatment was applied to the printed structures using a light-curing water-washable high-toughness acrylic resin infused with hydrophobic nanoparticles. Observations revealed that while the hexagonal interiors were filled with resin, the bridges and spikes retained their distinct geometries due to a thin resin coating on these surfaces. Stereomicroscope measurements confirmed that the treated structures had dimensions consistent with their untreated counterparts (Table S1), indicating that the superhydrophobic treatment did not significantly alter the structural integrity.

To evaluate durability, superhydrophobic-coated structures were subjected to 100 cycles of reciprocating friction tests. Post-test stereomicroscopic observations revealed

minimal changes in surface morphology compared to pre-test conditions. These findings were corroborated by digital microscopy measurements, which showed no significant dimensional changes in the structures (Table S1).

These results underscore the robustness of this biomimetic design and highlight the effectiveness of the superhydrophobic treatment in creating durable water-repellent surfaces. The fabricated structures successfully mimic the structural resilience observed in natural beehives and represent promising applications for bioinspired engineering solutions.

3.2. Surface wettability change before and after friction test

Surface wettability evaluations were performed on superhydrophobic-coated structures using 5 μL water droplets to determine contact angles (Figure 3). The results showed excellent superhydrophobicity for all designs, with contact angles consistently greater than 150°, regardless of the hexagonal area (Figure 3a). Detailed analysis of the droplet behavior during the measurements revealed exceptional hydrophobicity (Figure 3b). When the droplets were ejected from the syringe tip and pressed against the treated surfaces, they maintained their spherical shape without spreading. Upon retraction, the droplets adhered to the syringe tip, leaving no residual moisture on the surface. This behavior underscores the extremely low level of adhesion between the droplets and the treated surfaces. The superhydrophobic properties were further validated by sliding angle measurements. When the structures were tilted by as little as 10°, the water droplets immediately rolled off. This low sliding angle indicates minimal hysteresis and high water mobility on these surfaces. However, notable surface irregularities were observed in the 24 mm^2 hexagonal area condition that were not present in the larger structured. These irregularities, as evidenced by stereomicroscope observations, were due to inaccuracies in the 3D printing process for smaller structures. As a

result, the superhydrophobic coating was applied unevenly, resulting in a lower average contact angle and greater variability compared to other conditions. Collectively, these results confirm the effectiveness of the superhydrophobic treatment in producing highly hydrophobic surfaces over various hexagonal area designs. The remarkable non-wetting properties observed—characterized by high contact angles, low adhesion, and low sliding angles—highlight potential applications in self-cleaning, anti-fouling, and water-repellent technologies. However, the irregularities in the smallest hexagonal area (24 mm^2) highlight the need for optimization in coating processes for smaller scale structures to ensure uniform superhydrophobic performance.

Friction tests were performed on superhydrophobic structures under a vertical load of 100 g and 100 linear reciprocating cycles. Friction durability varied depending on the area of the outermost features of the structure (Figure 3). Overall, the bridge section retained its superhydrophobicity under most conditions after the friction test. In contrast, for the hexagonal regions, an optimal surface area condition was observed within the experimental friction parameters. Specifically, when the hexagonal area was 24 mm^2, the surface exhibited superhydrophobicity before the friction test but lost this property afterwards, with the contact angle decreasing to an average of 123°, the lowest of all tested conditions (Figure 3a). This loss of superhydrophobicity was attributed to surface irregularities resulting from inadequate 3D printing resolution at this scale (Figure 3b). The millimeter-scale unevenness resulted in localized load concentrations during friction, which caused the hydrophobic nanoparticles to detach from the surface. For larger surface areas of 40 mm^2 or more, the average contact angle showed a decreasing trend with increasing surface area after the friction test, especially within the hexagonal interiors. However, in the bridge region, no significant variation in contact angle was observed with increasing surface area, and the contact angle remained nearly constant. Among all conditions tested, the 40 mm^2 surface exhibited the highest

friction durability, retaining superhydrophobicity with a post-friction contact angle above 150°. Both the hexagonal interior and bridge (hexagonal outer shell) remained superhydrophobic. As shown in Figure 3b, even when a water droplet was pressed against the surface, it exhibited such strong hydrophobicity that it remained attached to the tip of the syringe needle without detaching. Similarly, the 80 mm^2 surface retained its superhydrophobicity throughout the surface even after the friction test. When the sliding angle was evaluated at a fixed substrate tilt of 10°, water droplets immediately rolled off the 40 mm^2 and 80 mm^2 surfaces, just as they did before the friction test. In contrast, the average values for the 120 mm^2 and 160 mm^2 surfaces dropped slightly below the superhydrophobic threshold. Water droplets detached from the syringe needle tip and adhered to certain regions of the surface, where they failed to roll off at a 10° slope and began to slide only at angles greater than 70°. This result suggests a transition from the lotus effect (Cassie-Baxter state) to the rose petal effect (Wenzel state) as the hexagonal surface area increases [38,39]. For the largest tested surface area tested, 200 mm^2, the surface failed to retain superhydrophobicity after the friction test, with the contact angle inside the hexagon decreasing significantly to an average of 139.5°. After friction, water droplets no longer followed the syringe needle tip, but instead detached and remained on the surface. Given that the contact area of the friction counterpart in the experiment was Φ15.3 mm, the results suggest that as the hexagonal surface area increased, the protective function of the PLA macrostructure in shielding the hydrophobic nanoparticles from friction decreased. In the 200 mm^2 condition, the hexagonal interior was in direct contact with the frictional counterpart without benefiting from the load distribution provided by the bridge region. This resulted in accelerated wear of the hexagonal interior, and especially, for the 200 mm^2 condition, the frictional counterpart penetrated the macrostructure's protective barrier, as one side of the hexagon measured only 8.48 mm before friction exposure.

For a more detailed assessment of the surface conditions before and after friction testing, 3D scanning laser microscopy was used to analyze the hexagonal interior (excluding the spike), bridge, and spike regions (Figures 4, S1, and S2). In the microscopy images, blue-white areas indicated the presence of hydrophobic nanoparticles. Before friction testing, all hexagonal surface conditions exhibited a similar coating of hydrophobic nanoparticles, with a pronounced accumulation around the bridge and spike regions. This pattern suggests a tendency for nanoparticles to concentrate in these areas during the squeegee coating process. When a superhydrophobic treatment coating was applied to the flat PLA surface, which has no macrostructure to provide protection, no uneven distribution of nanoparticles was observed, and the coating was uniform (Figure S7). Considering that the same uneven distribution was observed in all structural conditions, it is not due to the difficulty of the squeegee coating process on the structure, but rather, when the hydrophobic nanoparticles were coated, they accumulated in the bridge and spike areas due to surface tension.

Observations after the friction test revealed variations depending on the hexagonal size. In the 24 mm^2 condition, while the concentrated nanoparticle aggregates around the bridges and spikes dissipated, nanoparticles remained on the surface. The reduction in contact angle was attributed to localized loss of nanoparticles within millimeter-scale irregularities resulting from molding defects. In contrast, surfaces with 40 mm^2 and 80 mm^2 hexagonal areas showed minimal changes before and after the friction test, consistent with their retained superhydrophobic properties. For larger hexagonal areas (120 mm^2, 160 mm^2, and 200 mm^2), significant nanoparticle accumulation and clumping were observed in the bridge regions after friction, with the effect being most pronounced in the 200 mm^2 condition. 3D height analysis revealed prominently raised clumped areas in this case (Figure S2). In all conditions, the spike regions showed minimal changes, suggesting that nanoparticles from the hexagonal interiors (excluding the spike regions) were displaced by friction and subsequently

accumulated around the bridges. This observation suggests that increased nanoparticle aggregation around the bridges correlates with increased wear damage within the hexagonal interiors. These microscopy results are consistent with the wettability evaluation results (Figure 3), which showed a decrease in water droplet contact angles within the hexagonal interiors as the hexagonal area increased. The consistent contact angles observed in the bridge regions, regardless of hexagonal size, can be attributed to the retention and aggregation of hydrophobic nanoparticles in these areas.

3.3. Design considerations for superhydrophobicity and durability

We investigate the intricate relationship between surface structure design, superhydrophobicity, and durability using the Cassie-Baxter model [40,41], which is expressed as follows:

Cassie–Baxter model: $\cos\theta = f(1 + \cos\theta_Y) - 1$ [Equation 1]

where θ is the apparent contact angle, f is the liquid-solid contact fraction, and θ_Y is Young's contact angle (i.e., the intrinsic contact angle of the bulk material). The model shows that as f decreases, the influence of the bulk material hydrophobicity (θ_Y) on the total surface hydrophobicity (θ) decreases. This suggests that even if the surface hydrophobicity deteriorates due to wear, maintaining a sufficiently low f may allow the surface to retain its superhydrophobic properties and a high apparent contact angle. In the present study, the honeycomb-inspired 3D-printed surface structure was designed to protect the embedded hydrophobic nanoparticles from direct abrasion. To evaluate the wettability of a surface without hydrophobic nanoparticles, we coated PLA with a photocurable resin without hydrophobic components. The resulting contact angle was measured to be 9.3°, indicating

strong hydrophilicity (Figure S7). This finding implies that the primary cause of hydrophilicity due to frictional wear is the depletion of hydrophobic nanoparticles from the surface. To quantify the effect of wear on surface wettability, we formulated a model that expresses the increase in the exposed hydrophilic fraction due to surface abrasion, assuming a hexagonal geometric structure:

Liquid-solid contact fraction: $f_{abraded} = \frac{\frac{3\sqrt{3}}{2}\left\{\left[(l_{in}\times\cos\frac{60^\circ}{2}+\frac{w}{2})\times\tan\frac{60^\circ}{2}\right]\times 2\right\}^2 - \frac{3\sqrt{3}}{2}{l_{in}}^2+\pi r^2\times 7}{\frac{3\sqrt{3}}{2}\left\{\left[(l_{in}\times\cos\frac{60^\circ}{2}+\frac{w}{2})\times\tan\frac{60^\circ}{2}\right]\times 2\right\}^2}$

[Equation 2]

where l_{in} is the length of the bridge, $\alpha = 60°$ is the internal angle of the triangle, w is the width of the bridge, and r is the radius of the spike tip (Figure 5a) [42,43]. The formula includes the outer hexagonal shell, the width of the outer hexagonal shell (halved due to the presence of adjacent hexagons), the inner region of the hexagon, and the total area of the seven spike tips. Accordingly, the length of one side of the hexagon, including the outer shell, is given by $\left[(l_{in} \times \cos\frac{60^\circ}{2} + \frac{w}{2}) \times \tan\frac{60^\circ}{2}\right] \times 2$, and the total area is obtained by $\frac{3\sqrt{3}}{2}\left\{\left[(l_{in} \times \cos\frac{60^\circ}{2} + \frac{w}{2}) \times \tan\frac{60^\circ}{2}\right] \times 2\right\}^2$. Similarly, the area of the inner hexagon is expressed as $\frac{3\sqrt{3}}{2}{l_{in}}^2$. The area of each spike tip is represented by πr^2.

In cases where the surface wettability deteriorates due to frictional wear, the contact angles for the abraded regions converge to those of the underlying coating material without hydrophobic nanoparticles. The contact angles for these abraded regions were determined to be $\theta_{abraded} = 110° \ (before\ friction)$ and $9.3° \ (after\ friction)$. The pre-friction value of 110° corresponds to the contact angle observed when hexamethyldisilazane−a surface modifier for hydrophobic nanoparticles—is applied to a flat surface. This value assumes that prior to friction, the surface of the structure is superhydrophobic due to the uniform coverage

of hydrophobic nanoparticles. Consequently, the contact angle of the hydrophobic nanoparticle coated regions was set to θ_{nano} = 110°. The post-friction value of 9.3° reflects the direct contact between water and the photocurable resin after the depletion of the hydrophobic nanoparticles. Based on these assumptions, we derived a theoretical equation that accounts for both abraded regions and nanoparticle-covered regions:

Theoretical contact angle: $\cos\theta = f_{abraded}(\cos\theta_{abraded} + 1) + f_{nano}(\cos\theta_{nano} + 1) - 1$

[Equation 3]

where $f_{abraded}$ is the liquid-solid contact fraction of the abraded region, $\theta_{abraded}$ is the corresponding contact angle, f_{nano} is the liquid-solid contact fraction of the nanostructures (set to 1% due to the small size and spherical morphology of the hydrophobic nanoparticles) [24], and θ_{nano} is the contact angle associated with the hydrophobic nanoparticles.

Figure 5b shows the graphical representation of Equation 3 using experimentally obtained values. Notably, according to the original 3D CAD design values, superhydrophobicity should theoretically persist regardless of friction (except for one condition: 24 mm^2 post-friction). However, as discussed earlier, the actual FDM 3D-printed structures deviate from their design values. In the fabricated samples, the bridge width increased and rounded formations appeared at the tip of the spikes, effectively increasing the top surface area of the lattice structure. As a result, the experimentally observed liquid-solid contact fractions for the 3D-printed structures were larger than the theoretical design values, resulting in a rightward shift of the plotted points in the graph.

Before the friction test, all hexagonal area conditions exhibited superhydrophobicity, with the experimentally measured contact angles exceeding the theoretical predictions. This discrepancy occurs because the superhydrophobic treatment ensures the presence of

hydrophobic nanoparticles on all top surfaces of the hexagonal structure, including the spike tips and bridge areas. This increased coverage of hydrophobic nanoparticles contributed to the observed superhydrophobicity. After frictional wear, surfaces with hexagonal areas of 40 mm^2 and 80 mm^2 retained superhydrophobicity. However, a closer examination of the theoretical curve shows that while the 40 mm^2 condition was close to the theoretical curve before friction, the 80 mm^2 condition was closer to the theoretical curve after friction. This suggests that at 40 mm^2, the hexagonal barrier effectively shielded the hydrophobic nanoparticles from wear, preserving their pre-friction state. In contrast, for surfaces with hexagonal areas of 120 mm^2 or greater, the deviation from the theoretical curve after friction increased as the area condition increased, indicating that wear progressed regardless of the protective function of the hexagonal barrier. For the 24 mm^2 condition, the drastic reduction in contact angle was attributed to the complete depletion of hydrophobic nanoparticles due to wear, compounded by deviations from the intended structural design.

These findings underscore the critical importance of minimizing the liquid-solid contact fraction while optimizing the shape and dimensions of the abraded surface to enhance wear resistance. A key design strategy is to develop structural configurations that effectively preserve hydrophobic nanoparticles, ensuring sustained superhydrophobicity even under frictional stress.

3.4. Durability against Continuous Friction and Wear

The long-term friction durability of the superhydrophobic surface structure was systematically evaluated by gradually increasing the number of friction test cycles (Figure 6). For comparative analysis, an initial friction test was conducted on a PLA surface without hexagonal structure but coated with photocurable resin and hydrophobic nanoparticles. The

surface exhibited an initial superhydrophobic state, with a contact angle of 165.1° (Figure S7). However, after only 10 friction test cycles, the contact angle dropped below the superhydrophobic threshold of 150°. After 200 cycles, the average contact angle further decreased to 110°. Hydrophilic behavior (contact angle < 90°) was observed after 400 cycles, with the contact angle stabilizing at approximately 45° after 800 cycles. These results emphasize that superhydrophobicity cannot be maintained in the absence of the protective honeycomb structure, even when hydrophobic nanoparticles are anchored by light-curing resin.

In contrast, the 40 mm^2 honeycomb surface showed significantly better frictional durability. It retained superhydrophobicity up to 200 cycles, significantly outperforming the unstructured surface. At 400 cycles, although the bridge section remained hydrophobic, the contact angle inside the honeycomb structure decreased to 117°. Beyond 400 cycles, the contact angle continued to decrease until it reached approximately 65° at 1000 cycles. Consistent with previous experiments on different hexagonal areas, the bridge section consistently exhibited higher contact angles than the honeycomb interior. These results indicate that the honeycomb architecture effectively mitigates the detachment of hydrophobic nanoparticles and preserves the hydrophobicity of the surface even in prolonged friction tests.

In this study, the inner region was intentionally composed of hydrophilic photocurable resin to demonstrate the protective role of the honeycomb barrier in maintaining superhydrophobicity. Future research could explore the potential for improving long-term frictional durability by using more robust resin formulations for the inner structure. This aspect provides an opportunity for further advances in the development of wear-resistant superhydrophobic surfaces. The results highlight the critical role of structural design in maintaining superhydrophobic properties under sustained friction conditions. The honeycomb structure not only provides an initial protective function, but also influences the rate of

superhydrophobic degradation, providing valuable insights for designing more resilient hydrophobic surfaces in practical applications. In addition, the practical applications of the developed superhydrophobic 3D-printed structures are detailed in the Supporting Information (Figure S9). These include demonstrations of architectural models and transparent superhydrophobic surfaces, highlighting their potential utility in various industries.

4. Conclusions

This research successfully demonstrated a novel approach for creating durable superhydrophobic surfaces on 3D-printed structures by mimicking beehive architectures. The study found that hexagonal macrostructures with surface areas between 40 mm^2 and 80 mm^2 provide optimal protection for hydrophobic nanoparticles, allowing them to retain their superhydrophobicity even after extensive friction testing under the experimental conditions presented in this work. The theoretical model, derived from the Cassie-Baxter equation, effectively elucidated the relationship between structural design and superhydrophobic performance. Furthermore, the study demonstrated practical applications of this technology, including its incorporation into architectural models and transparent superhydrophobic structures. These findings open new avenues for incorporating durable superhydrophobic properties into a variety of 3D-printed products, potentially revolutionizing industries such as construction, automotive engineering, and optics. Future research directions could focus on improving the long-term durability of these surfaces by using more robust resin formulations and expanding the range of applications that take advantage of the synergy between 3D printing and superhydrophobic functionality. Overall, this study represents a significant advancement in the development of wear-resistant, water-repellent materials for additive

manufacturing technologies and offers promising prospects for future innovations in functional surface engineering.

ASSOCIATED CONTENT

Supporting Information

The following Supporting Information is available free of charge.

Funding Sources

JSPS KAKENHI Grant Number JP23K17822, Suzuki Foundation 2022 Science and Technology Research Grant Number 29.

Notes

The authors declare no competing financial interests.

ACKNOWLEDGMENTS

This work was supported by JSPS KAKENHI Grant Number JP23K17822, and the Suzuki Foundation 2022 Science and Technology Research Grant Number 29. We would like to express our sincere gratitude to Mr. Tetsuhiro Iwai, who contributed to this study during his internship from the Department of Applied Chemistry and Life Science, Toyohashi University of Technology. Special thanks are extended to Prof. Dr. Akihiko Matsumoto (Toyohashi University of Technology) for his invaluable guidance as Mr. Iwai's supervisor.

References

[1] MacDonald E, Wicker R. Multiprocess 3D printing for increasing component functionality. *Science*. 2016;353(6307):aaf2093-aaf2093. doi:10.1126/science.aaf2093

[2] Ligon SC, Liska R, Stampfl J, et al. Polymers for 3D Printing and Customized Additive Manufacturing. *Chem Rev.* 2017;117(15):10212-10290. doi:10.1021/acs.chemrev.7b00074

[3] Gul JZ, Sajid M, Rehman MM, et al. 3D printing for soft robotics - a review. *Sci Technol Adv Mater.* 2018;19(1):243-262. doi:10.1080/14686996.2018.1431862

[4] Olawumi MA, Oladapo BI, Ikumapayi OM, et al. Waste to wonder to explore possibilities with recycled materials in 3D printing. *Sci Total Environ.* 2023;905(167109):167109. doi:10.1016/j.scitotenv.2023.167109

[5] Voet VSD, Guit J, Loos K. Sustainable photopolymers in 3D printing: A review on biobased, biodegradable, and recyclable alternatives. *Macromol Rapid Commun.* 2021;42(3):2000475. doi:10.1002/marc.202000475

[6] Tay YWD, Panda B, Paul SC, et al. 3D printing trends in building and construction industry: a review. *Virtual Phys Prototyp.* 2017;12(3):261-276. doi:10.1080/17452759.2017.1326724

[7] Mohanavel V, Priyadharshan R, Ravichandran M, et al. The role and application of 3D printer in the automobile industry. *ECS Trans.* 2022;107(1):12001-12010. doi:10.1149/10701.12001ecst

[8] Tenjimbayashi M, Manabe K. A review on control of droplet motion based on wettability modulation: principles, design strategies, recent progress, and applications. *Sci Technol Adv Mater.* 2022;23(1):473-497. doi:10.1080/14686996.2022.2116293

[9] Feng L, Li S, Li Y, et al. Super - hydrophobic surfaces: From natural to artificial. *Adv Mater.* 2002;14(24):1857-1860. doi:10.1002/adma.200290020

[10] Xue CH, Jia ST, Zhang J, et al. Large-area fabrication of superhydrophobic surfaces for practical applications: an overview. *Sci Technol Adv Mater.* 2010;11(3):033002. doi:10.1088/1468-6996/11/3/033002

[11] Barthlott W, Neinhuis C. Purity of the sacred lotus, or escape from contamination in biological surfaces. *Planta.* 1997;202(1):1-8. doi:10.1007/s004250050096

[12] Lafuma A, Quéré D. Superhydrophobic states. *Nat Mater.* 2003;2(7):457-460. doi:10.1038/nmat924

[13] Xuan S, Yin H, Li G, et al. Trifolium repens L.-like periodic micronano structured superhydrophobic surface with ultralow ice adhesion for efficient anti-icing/deicing. *ACS Nano.* 2023;17(21):21749-21760. doi:10.1021/acsnano.3c07385

[14] Zhang H, Lamb R, Lewis J. Engineering nanoscale roughness on hydrophobic surface—preliminary assessment of fouling behaviour. *Sci Technol Adv Mater.* 2005;6(3-4):236-239. doi:10.1016/j.stam.2005.03.003

[15] Manabe K, Nishizawa S, Kyung KH, et al. Optical phenomena and antifrosting property on biomimetics slippery fluid-infused antireflective films via layer-by-layer comparison with superhydrophobic and antireflective films. *ACS Appl Mater Interfaces.* 2014;6(16):13985-13993. doi:10.1021/am503352x

[16] Barraza B, Olate-Moya F, Montecinos G, et al. Superhydrophobic SLA 3D printed materials modified with nanoparticles biomimicking the hierarchical structure of a rice leaf. *Sci Technol Adv Mater.* 2022;23(1):300-321. doi:10.1080/14686996.2022.2063035

[17] Su Y, Ji B, Zhang K, et al. Nano to micro structural hierarchy is crucial for stable superhydrophobic and water-repellent surfaces. *Langmuir.* 2010;26(7):4984-4989. doi:10.1021/la9036452

[18] Teisala H, Tuominen M, Aromaa M, et al. Nanostructures increase water droplet adhesion on hierarchically rough superhydrophobic surfaces. *Langmuir.* 2012;28(6):3138-3145. doi:10.1021/la203155d

[19] Verho T, Bower C, Andrew P, et al. Mechanically durable superhydrophobic surfaces. *Adv Mater.* 2011;23(5):673-678. doi:10.1002/adma.201003129

[20] Yokoi N, Manabe K, Tenjimbayashi M, et al. Optically transparent superhydrophobic surfaces with enhanced mechanical abrasion resistance enabled by mesh structure. *ACS Appl Mater Interfaces.* 2015;7(8):4809-4816. doi:10.1021/am508726k

[21] Li T, Peng Y, You H, et al. Yang C. Recent developments in the fabrication and application of superhydrophobic suraces. *Chem Rec.* 2024;24(9):e202400065. doi:10.1002/tcr.202400065

[22] Tian J, Qi X, Li C, et al. Mussel-Inspired Fabrication of an Environment-Friendly and Self-Adhesive Superhydrophobic Polydopamine Coating with Excellent Mechanical Durability, Anti-Icing and Self-Cleaning Performances. *ACS Appl Mater Interfaces.* 2023;15(21):26000-26015. doi:10.1021/acsami.3c03577

[23] Jiang J, Shen Y, Wang Z, et al. Design and fabrication superhydrophobic surface with enhanced mechanical durability: Interface bonding effects regulated by an introduced

transition oxide layer. *Appl Surf Sci.* 2022;592(153199):153199. doi:10.1016/j.apsusc.2022.153199

[24] Wang D, Sun Q, Hokkanen MJ, et al. Design of robust superhydrophobic surfaces. *Nature*. 2020;582(7810):55-59. doi:10.1038/s41586-020-2331-8

[25] He Y, Wang L, Wu T, et al. Facile fabrication of hierarchical textures for substrate-independent and durable superhydrophobic surfaces. *Nanoscale*. 2022;14(26):9392-9400. doi:10.1039/d2nr02157a

[26] Wei J, Li B, Tian N, et al. Scalable robust superamphiphobic coatings enabled by self - similar structure, protective micro - skeleton, and adhesive for practical anti - icing of high - voltage transmission tower. *Adv Funct Mater*. 2022;32(43):2206014. doi:10.1002/adfm.202206014

[27] Yamauchi Y, Tenjimbayashi M, Samitsu S, et al. Durable and Flexible Superhydrophobic Materials: Abrasion/Scratching/Slicing/Droplet Impacting/Bending/Twisting-Tolerant Composite with Porcupinefish-Like Structure. *ACS Appl Mater Interfaces.* 2019;11(35):32381-32389. doi:10.1021/acsami.9b09524

[28] Wu Z, Shi C, Chen A, et al. Large-Scale, Abrasion-Resistant, and Solvent-Free Superhydrophobic Objects Fabricated by a Selective Laser Sintering 3D Printing Strategy. *Adv Sci.* 2023;10(9):2207183. doi:10.1002/advs.202207183

[29] Amin M, Singh M, Ravi KR. Fabrication of superhydrophobic PLA surfaces by tailoring FDM 3D printing and chemical etching process. *Appl Surf Sci.* 2023;626(157217):157217. doi:10.1016/j.apsusc.2023.157217

[30] Manabe K, Saikawa M, Sato I, et al. Biomimetic 3D-printed armored structures for durable superhydrophobic surfaces: Integrating macroprotection and nanofunctionality. *ACS Appl Polym Mater.* 2024;6(22):13701-13709. doi:10.1021/acsapm.4c02416

[31] Dong Z, Vuckovac M, Cui W, et al. 3D Printing of Superhydrophobic Objects with Bulk Nanostructure. *Adv Mater.* 2021;33(45):2106068. doi:10.1002/adma.202106068

[32] Otis GW, Smith DR. Drone cell cappings of Asian cavity-nesting honey bees (Apis spp.). *Apidologie*. 2021;52(4):782-791. doi:10.1007/s13592-021-00864-8

[33] Kubásek J, Svobodová K, Půta F, et al.Honeybees control the gas permeability of brood and honey cappings. *iScience*. 2022;25(11):105445. doi:10.1016/j.isci.2022.105445

[34] Drumright RE, Gruber PR, Henton DE. Polylactic acid technology. *Adv Mater.* doi:10.1002/1521-4095(200012)12:23<1841::AID-ADMA1841>3.0.CO;2-E

[35] Agbakoba VC, Webb N, Jegede E, et al. Mechanical recycling of waste PLA generated from 3D printing activities: Filament production and thermomechanical analysis. *Macromol Mater Eng.* 2024;309(8):2300276. doi:10.1002/mame.202300276

[36] Shi C, Quinn EC, Diment WT, et al. Recyclable and (Bio)degradable Polyesters in a Circular Plastics Economy. *Chem Rev.* 2024;124(7):4393-4478. doi:10.1021/acs.chemrev.3c00848

[37] Tamir TS, Xiong G, Fang Q, et al. A feedback-based print quality improving strategy for FDM 3D printing: an optimal design approach. *Int J Adv Manuf Technol.* 2022;120(3):2777-2791. doi:10.1007/s00170-021-08332-4

[38] Sun S, Li H, Guo Y, et al. Superefficient and robust polymer coating for bionic manufacturing of superwetting surfaces with “rose petal effect” and “lotus leaf effect.” *Prog Org Coat.* 2021;151(106090):106090. doi:10.1016/j.porgcoat.2020.106090

[39] Chen S, Zhu M, Zhang Y, et al. Magnetic-responsive superhydrophobic surface of magnetorheological elastomers mimicking from lotus leaves to Rose petals. *Langmuir*. 2021;37(7):2312-2321. doi:10.1021/acs.langmuir.0c03122

[40] Erbil HY, Cansoy CE. Range of applicability of the Wenzel and Cassie-Baxter equations for superhydrophobic surfaces. *Langmuir.* 2009;25(24):14135-14145. doi:10.1021/la902098a

[41] Park IW, Ribe JM, Fernandino M, et al. The criterion of the Cassie–Baxter and Wenzel wetting modes and the effect of elastic substrates on it. *Adv Mater Interfaces*. 2023;10(12):2202439. doi:10.1002/admi.202202439

[42] Lepikko S, Turkki V, Koskinen T, et al. Droplet friction on superhydrophobic surfaces scales with liquid-solid contact fraction. *Small*. 2024:2405335. doi:10.1002/smll.202405335

[43] Zhang D, Takase S, Nagayama G. Measurement of effective wetting area at hydrophobic solid-liquid interface. *J Colloid Interface Sci.* 2021;591:474-482. doi:10.1016/j.jcis.2021.01.056

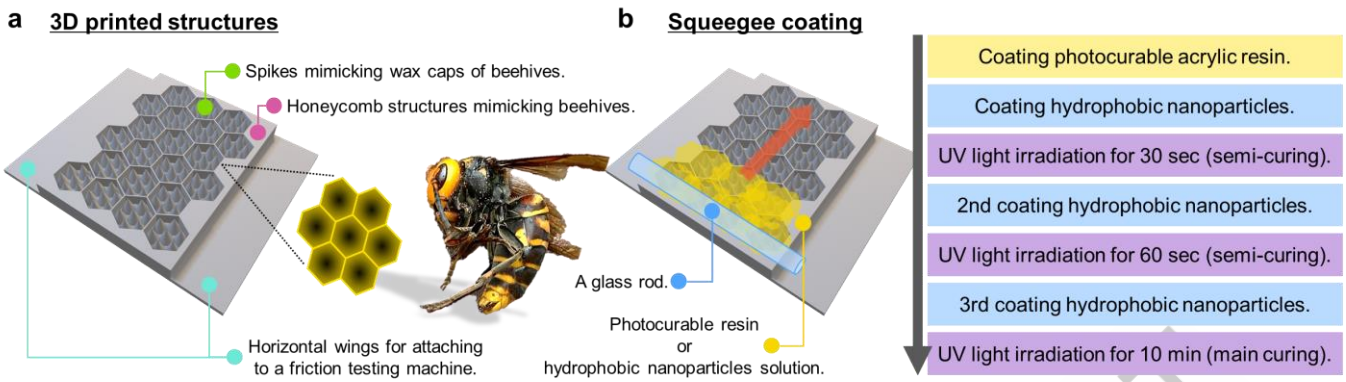

Figure 1. Schematic diagram of the research concept and overall experimental process. Schematic of (a) 3D printed structures and (b) squeegee coating process with flowchart of the superhydrophobic treatment method. (a) Beehive-inspired honeycomb macrostructures are fabricated using a FDM 3D printer with PLA filament to protect the hydrophobic nanostructures inside. (b) For superhydrophobic treatment, the squeegee coating process was applied via layer-by-layer. UV-photocurable resin was squeegee coated to the surface of the 3D printed structures (first step). Before the photocurable resin cured, hydrophobic nanoparticles were squeegee coated onto the surface (second step); UV light irradiation was applied to cure the photocurable resin (third step). Similarly, the second and third layers were coated with hydrophobic nanoparticles. Detailed procedures and information on UV exposure times are provided in the flowchart and the experimental section.

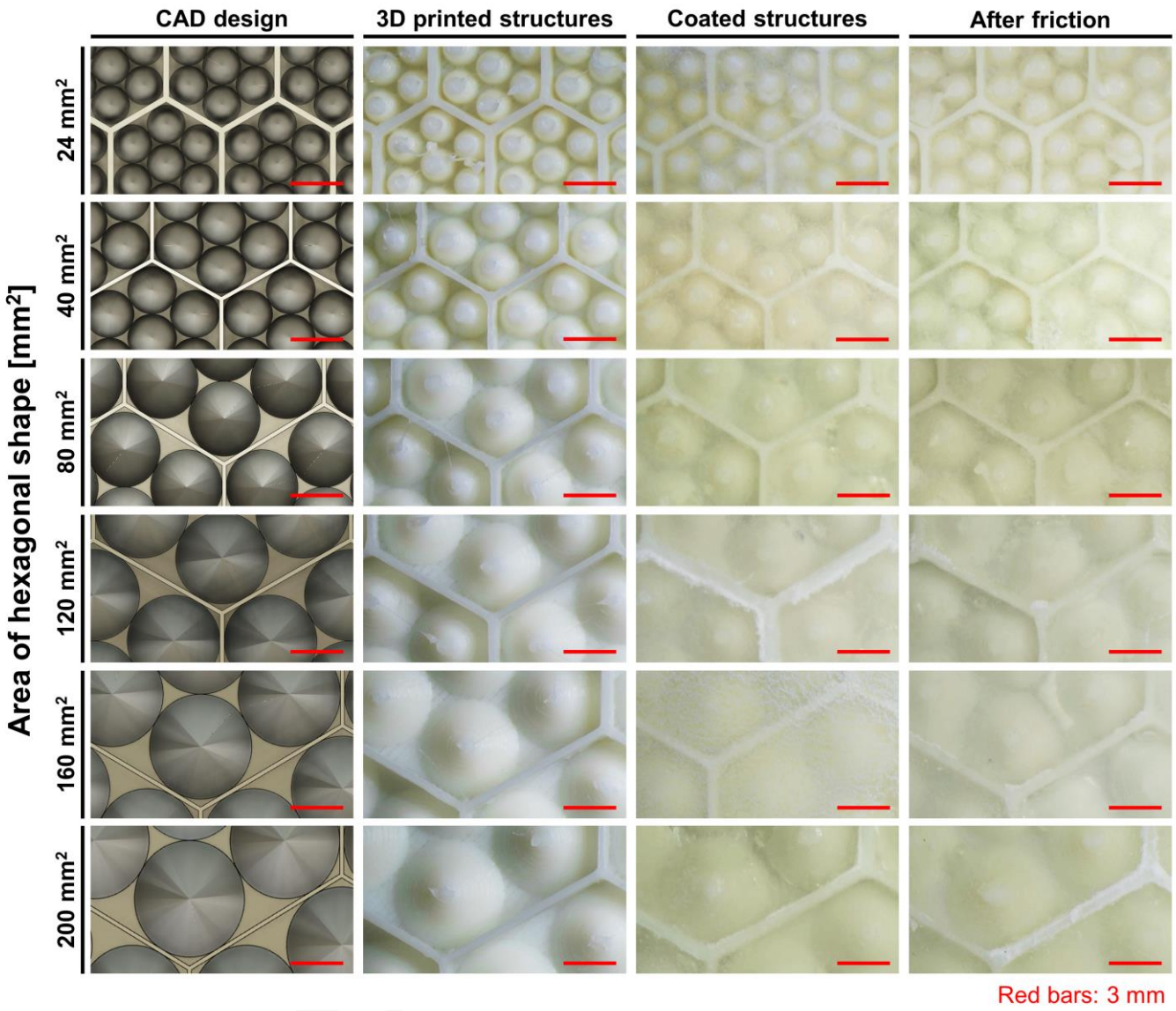

Figure 2: Surface structure through 3D printing and coating processes. The columns, from left to right, show: the initial structure designed by 3D CAD software (CAD design), the structure as fabricated by a 3D printer based on the CAD model, the structure after application of a superhydrophobic coating, and the surface of the coated structure after friction test. The friction test was performed by reciprocating 100 times, and the other friction conditions are as described in the experimental section. All structures, except for the CAD design, were observed and imaged using a stereo microscope equipped with a digital microscope camera. The red scale bars in all images represent 3 mm.

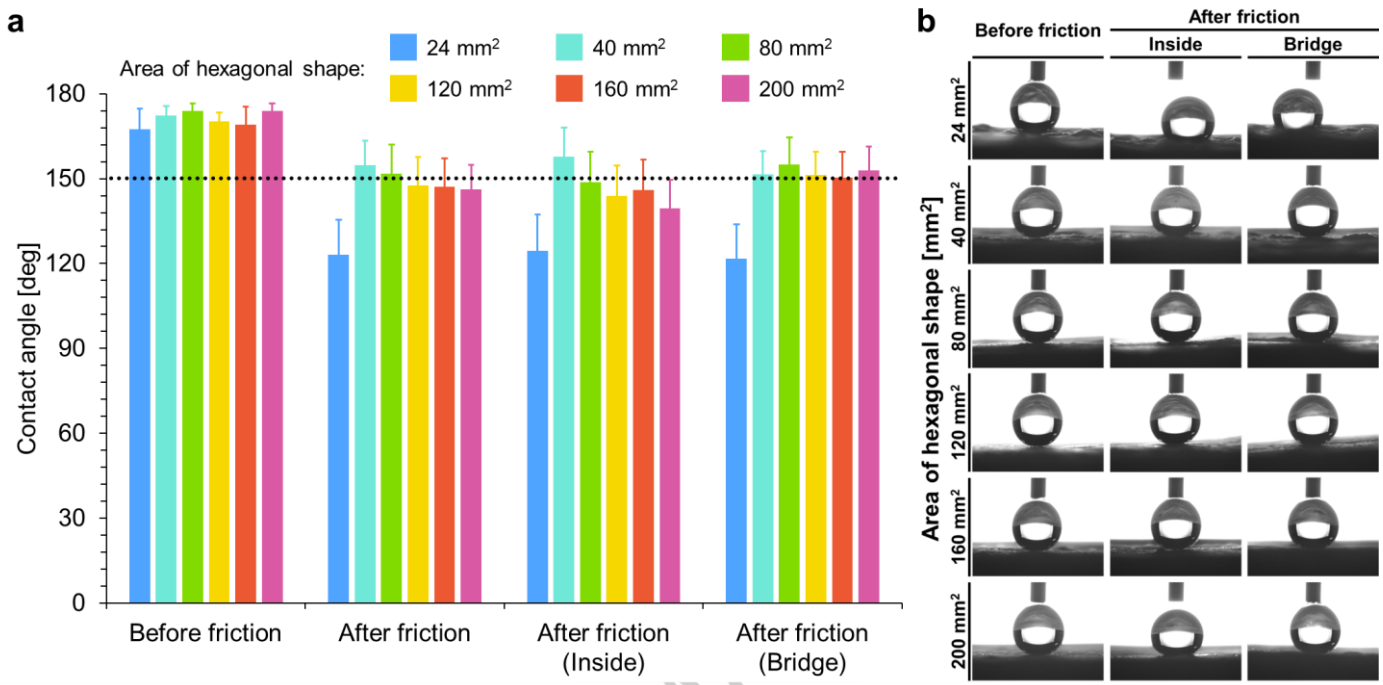

Figure 3. Surface wettability evaluation. (a) Contact angle measurements of 5 µL water droplets before and after the friction durability test. The friction test consisted of 100 reciprocating cycles under the conditions described in the experimental section. The post-friction test results are shown for the hexagon inside, the bridge (outer shell of the hexagon), and the overall average. The black dotted line at 150° indicates the threshold for superhydrophobicity. (b) Representative images of 5 µL water droplets during contact angle measurements before and after the friction durability test. Post-friction images illustrate the droplet behavior on the hexagon inside and bridge structures.

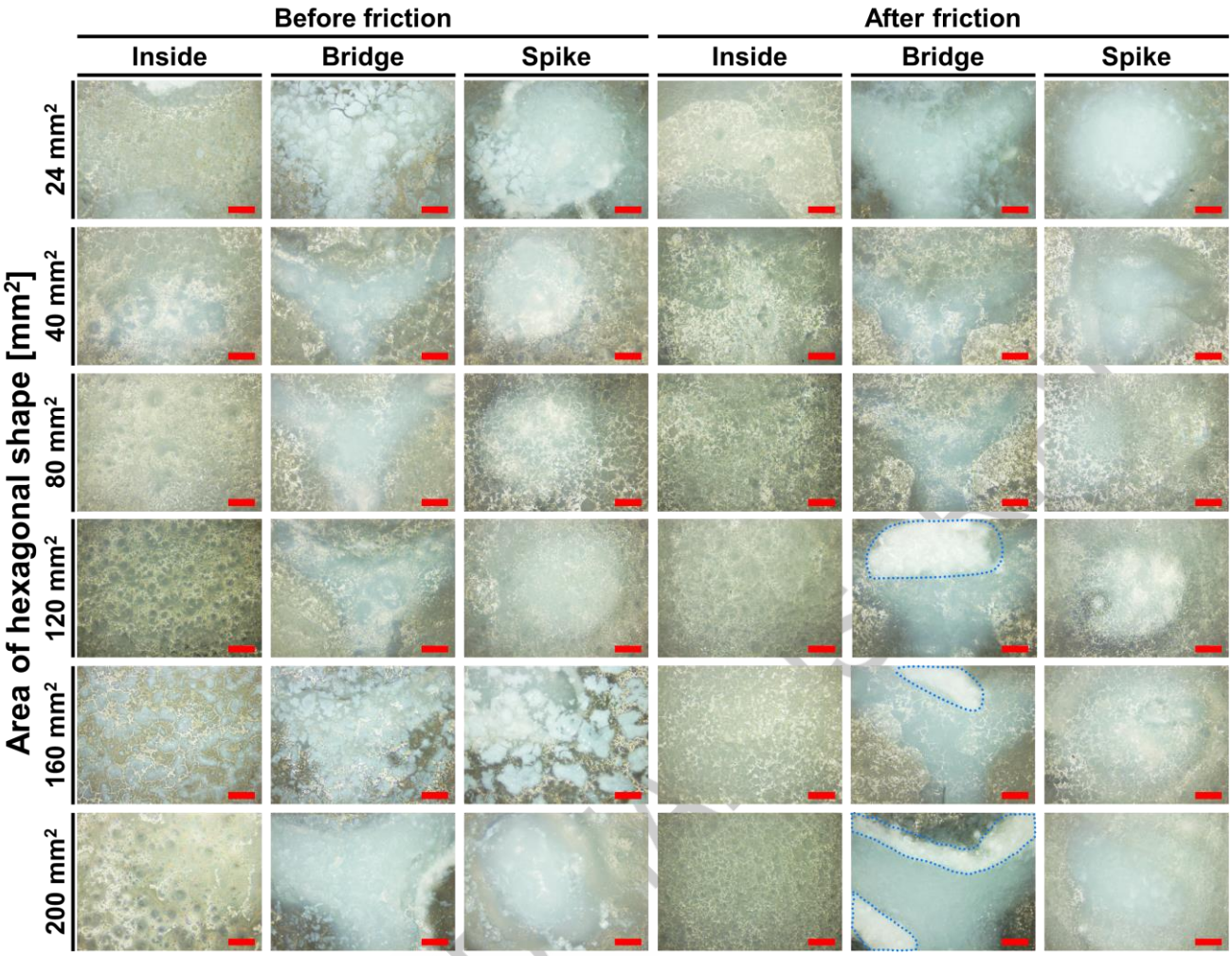

Figure 4. Surface morphology changes before and after friction durability testing. Images were obtained using a 3D scanning laser microscope. Blue-white regions indicate the presence of hydrophobic nanoparticles. The area surrounded by the blue dotted line is where the hydrophobic nanoparticles are highly aggregated. All images share a 200 μm scale bar (red). Optical microscope images were primarily used for color assessment to confirm the presence of hydrophobic nanoparticles. Corresponding laser reflection/optical microscope composite images and 3D height observation images, detailing changes in surface roughness before and after the friction durability test are shown in Figures S1 and S2. The friction test consisted of 100 reciprocating cycles under conditions detailed in the experimental section.

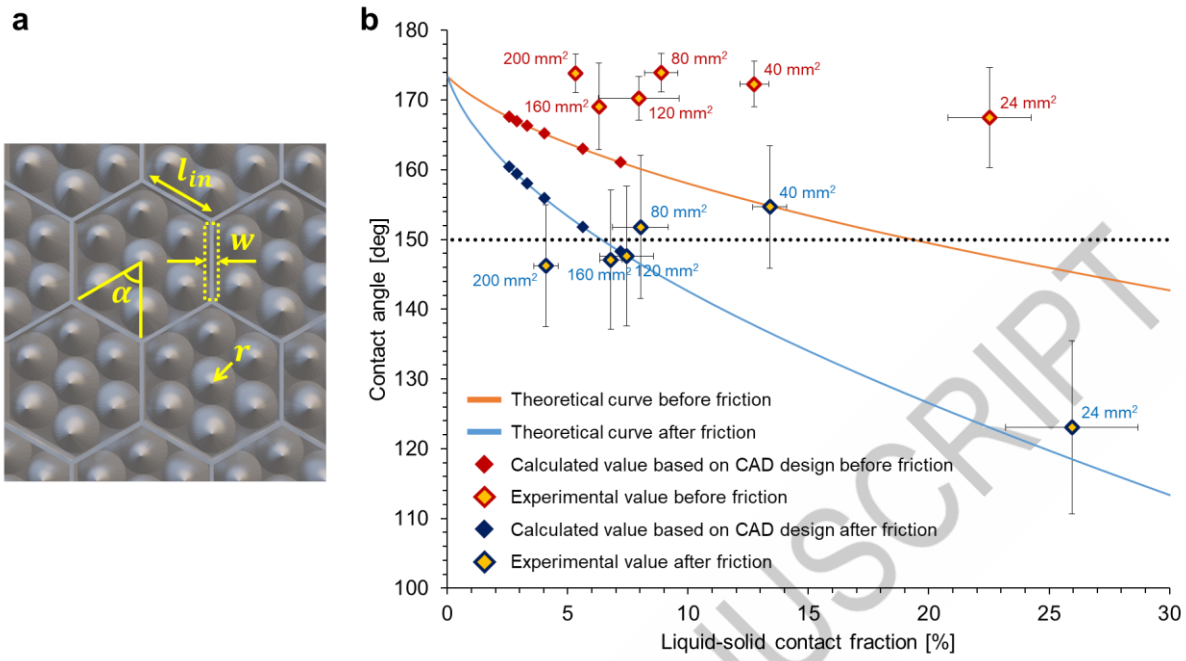

Figure 5. Surface structure parameters and wettability analysis. (a) Schematic representation of the design parameters used in the theoretical equation: bridge length (l_{in}), internal angle (α), bridge width (w), and spike apex radius (r). (b) Comparison between theoretical model predictions and experimental contact angle measurements before and after frictional wear. The theoretical curves derived from equation (3) are represented by orange (before friction) and light blue (after friction) lines. Red and blue diamonds indicate calculated values based on design parameters before and after friction, respectively. Yellow diamonds surrounded by red and blue frames represent experimentally obtained values before and after friction, respectively. The black dotted line at 150° indicates the threshold for superhydrophobicity.

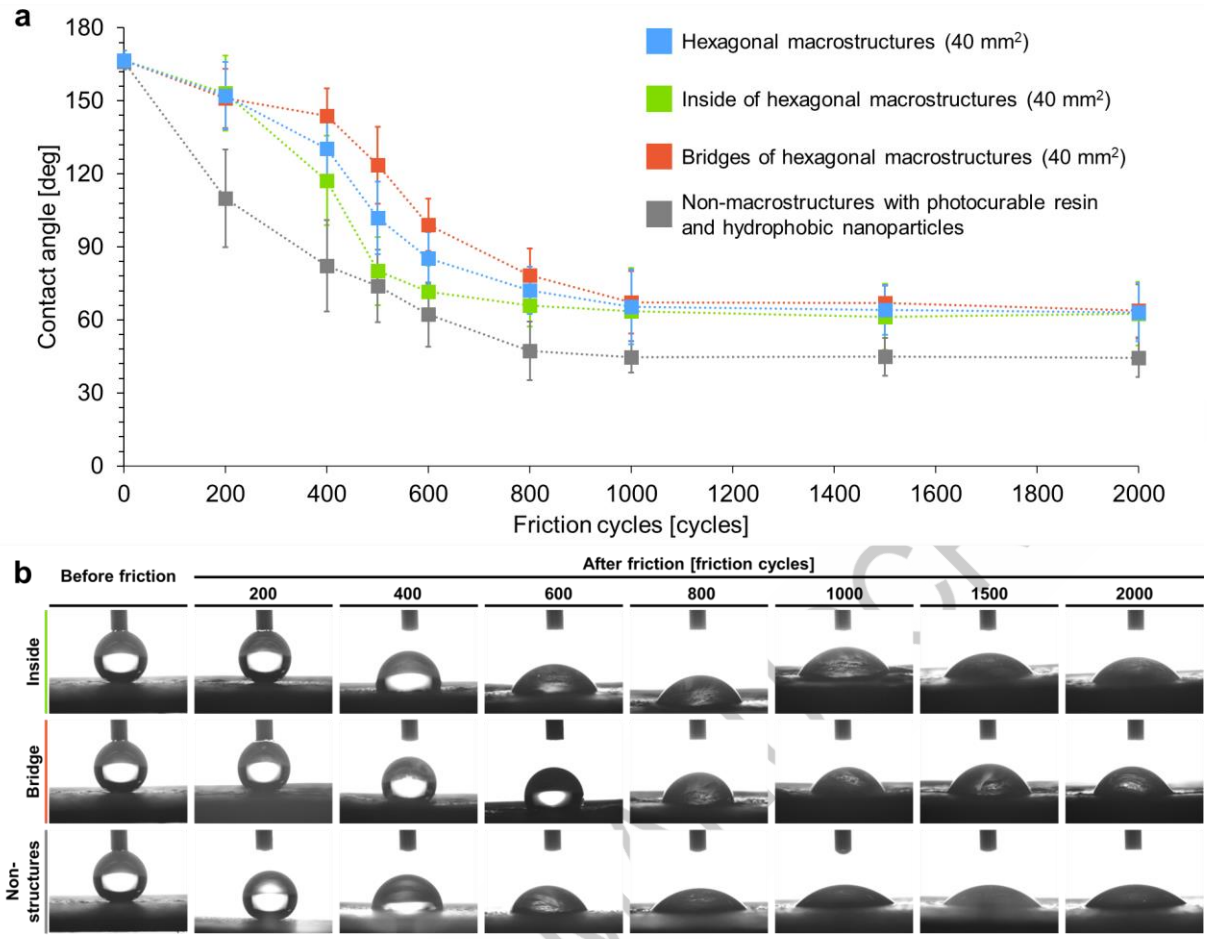

Figure 6. Long-term friction durability test of superhydrophobic surfaces. (a) Evolution of contact angle with increasing number of friction cycles. The graph compares the performance of surfaces with and without hexagonal barrier macrostructures. For the hexagonal barrier structure, separate measurements are shown for the honeycomb interior (green squares), the bridge section (red squares), and their average (blue squares). A surface without the barrier macrostructure, coated only with hydrophobic nanoparticles and resin, serves as a control (gray squares). (b) Representative images of 5 μL water droplets corresponding to the contact angle measurements in (a). The images illustrate the changes in droplet shape and contact angle as the number of friction cycles increases. The friction test conditions, except for the number of cycles, were the same as those described in the experimental section.

[[Graphical Abstract]]

Impact Statement

The study introduces an approach to creating durable superhydrophobic surfaces combining hydrophobic nanoparticles protected by 3D-printed hexagonal macrostructures inspired by beehive architecture, enhancing durability while maintaining superhydrophobicity under mechanical stress.

Supporting Information

Durable Superhydrophobic Surfaces on 3D-Printed Structures Inspired by Beehive Architecture

Kengo Manabe, Makoto Saikawa, Tetsuhiro Iwai, and Yasuo Norikane*

Correspondence email: kengo.manabe@aist.go.jp*

Supporting Information contains:

Supporting Figures

Figure S1. Composite laser reflection and optical microscope images before and after the friction test

Figure S2. Surface height and roughness evaluation before and after the friction test

Figure S3. Stereomicroscope images of 3D-printed structures with bridge widths of (a) 0.5 mm and (b) 0.2 mm

Figure S4. Comparison of surface wettability in 3D-printed structures with varying bridge widths

Figure S5. 3D-printed structures with varying spike geometries

Figure S6. Surface wettability comparison of 3D-printed structures with different spike shapes

Figure S7. Surface wettability changes of various coatings without honeycomb-structured barriers

Figure S8. Comparison of friction durability with and without spikes

Figure S9. Practical applications of 3D-printed superhydrophobic surfaces

Supporting Table

Table S1. Design and measured values of hexagonal shapes of structural surfaces designed by 3D CAD, 3D printed structures, and coated structures before and after friction test

Table S2. Comprehensive comparison of superhydrophobic surfaces fabricated using various 3D printing methods and materials, with a focus on their durability

Supporting References

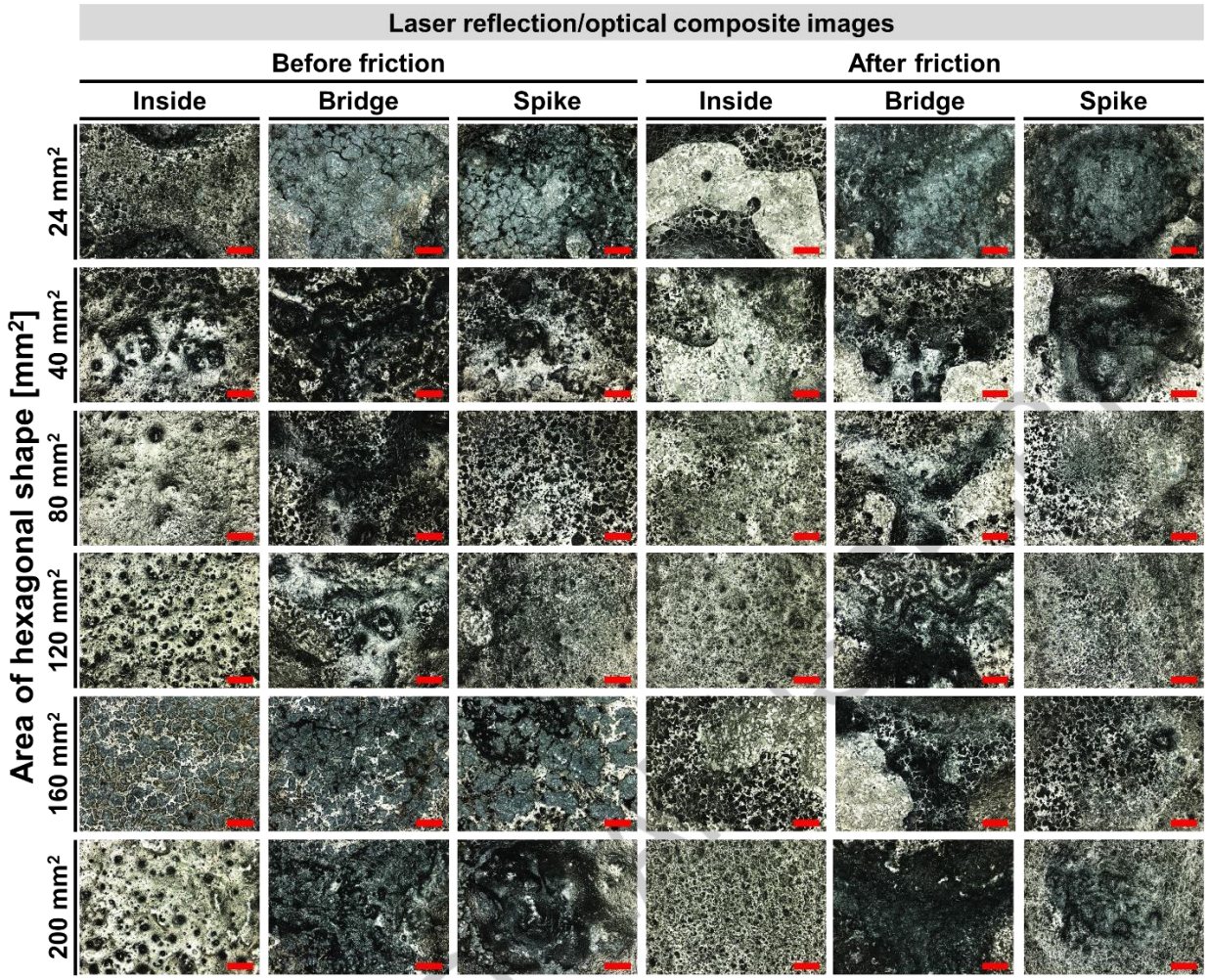

Figure S1. Composite laser reflection and optical microscope images before and after the friction test. The images, obtained using 3D scanning laser microscopy, provide both color and surface topography information. All red scale bars represent 200 µm.

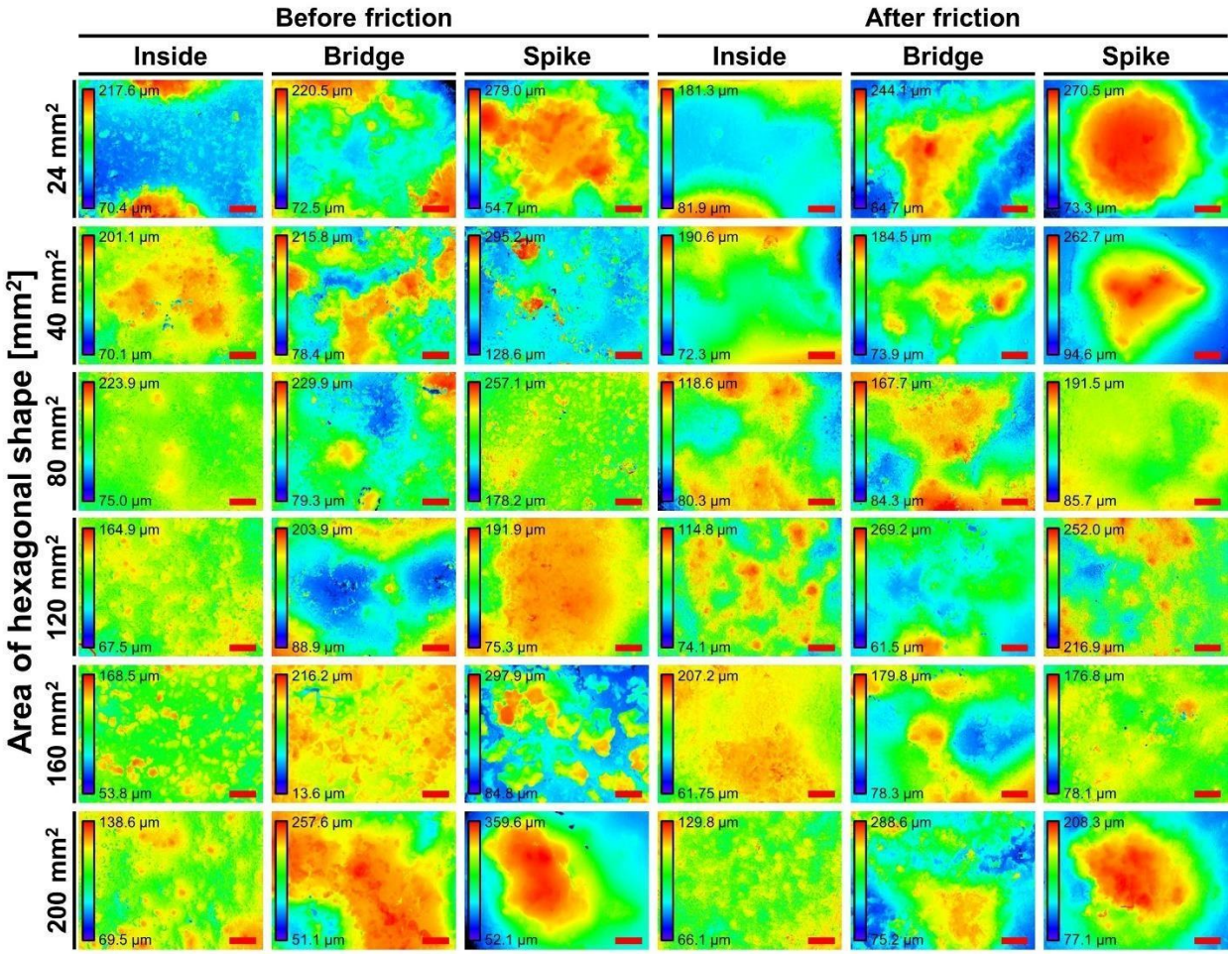

Figure S2. Surface height and roughness evaluation before and after the friction test. 3D scanning laser microscopy was used to evaluate surface height and roughness before and after the friction durability test. All red scale bars represent 200 µm.

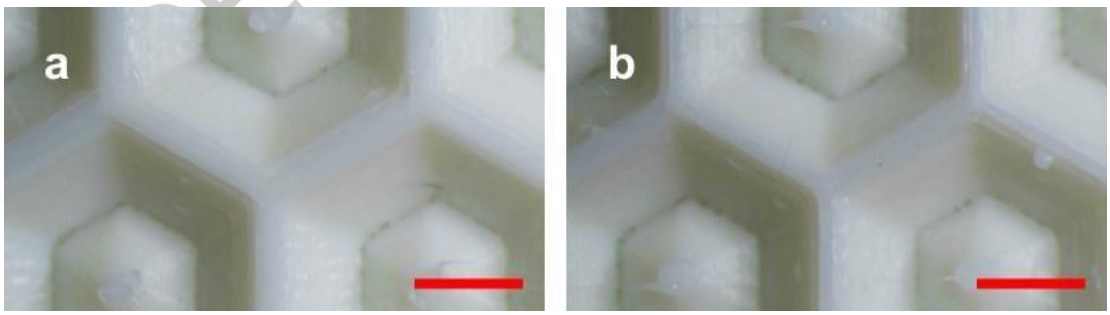

Figure S3. Stereomicroscope images of 3D-printed structures with bridge widths of (a) 0.5 mm and (b) 0.2 mm. All red scale bars represent 3 mm. The number of spikes was restricted to one to minimize the influence of defective spike molding on the intended bridge width.

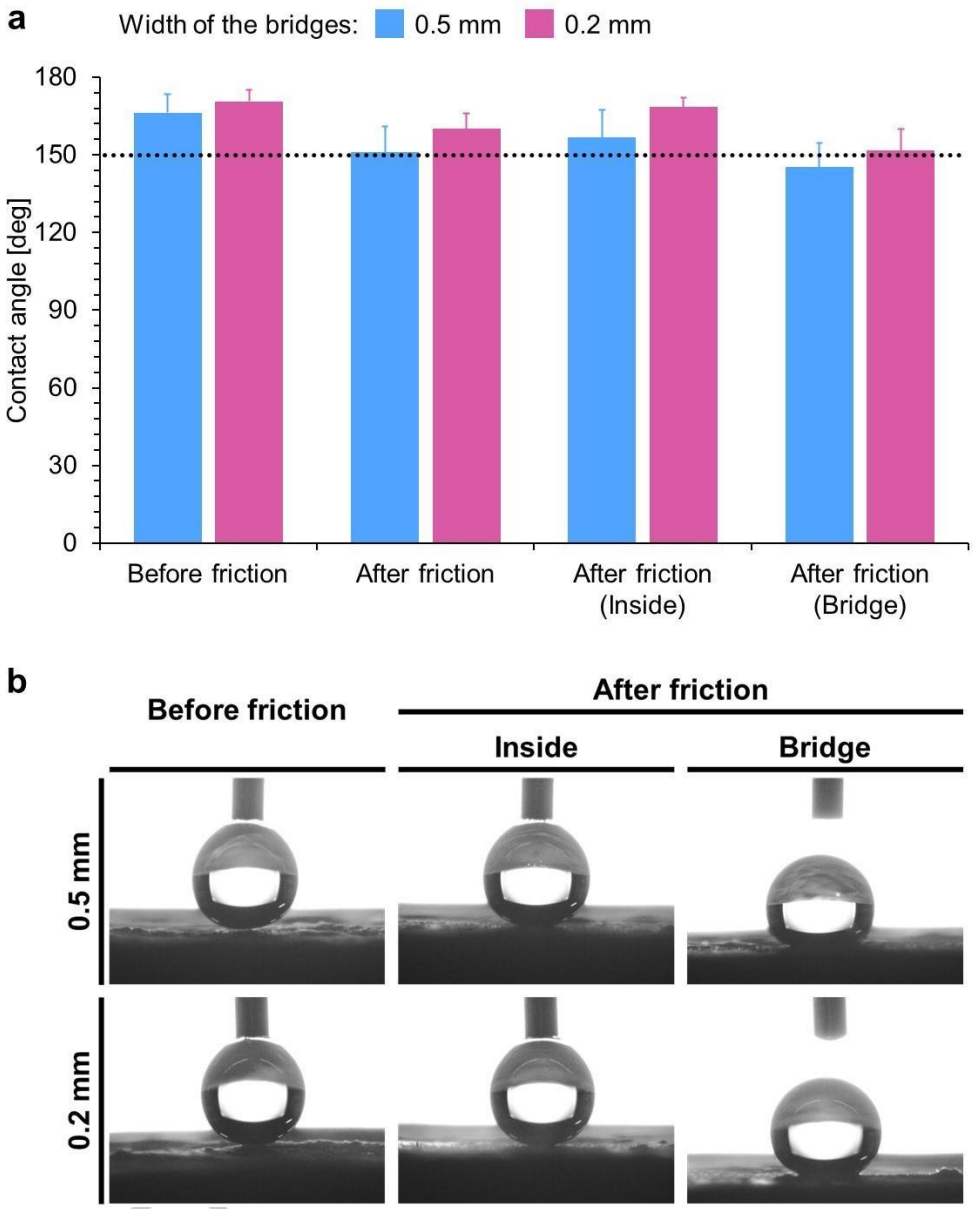

Figure S4. Comparison of surface wettability in 3D-printed structures with varying bridge widths. (a) Contact angle measurements of 5 µL water droplets on two types of 3D-printed structures with different bridge widths, before and after friction durability testing. The friction test involved 100 reciprocating cycles under the conditions specified in the experimental section. Results are presented for the hexagon interior, the bridge (outer shell of the hexagon), and the overall average. The black dotted line at 150° indicates the superhydrophobicity threshold. (b) Representative images of 5 µL water droplets captured during contact angle measurements before and after friction durability testing. The images show the droplet behavior on the hexagon interior and bridge structures for both bridge width configurations.

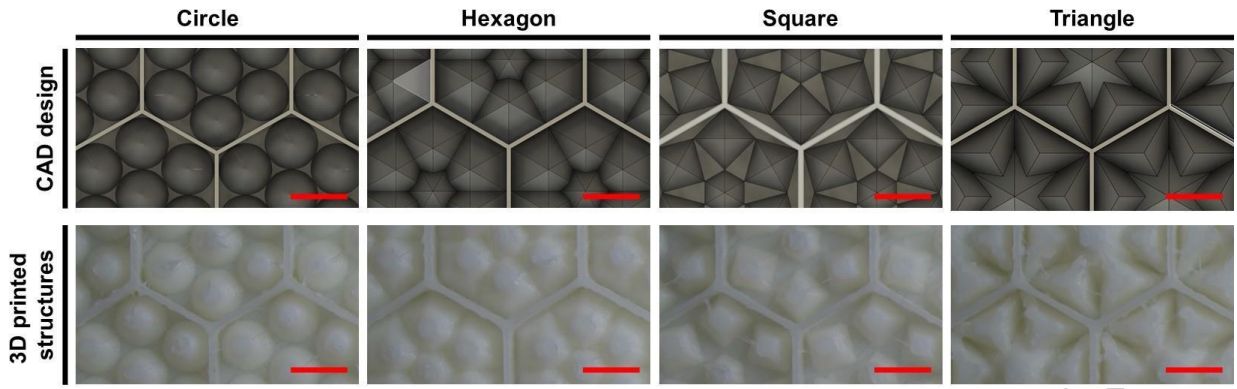

Figure S5. 3D-printed structures with varying spike geometries. CAD models and corresponding 3D-printed results observed under a stereomicroscope. Red scale bars in all images represent 3 mm.

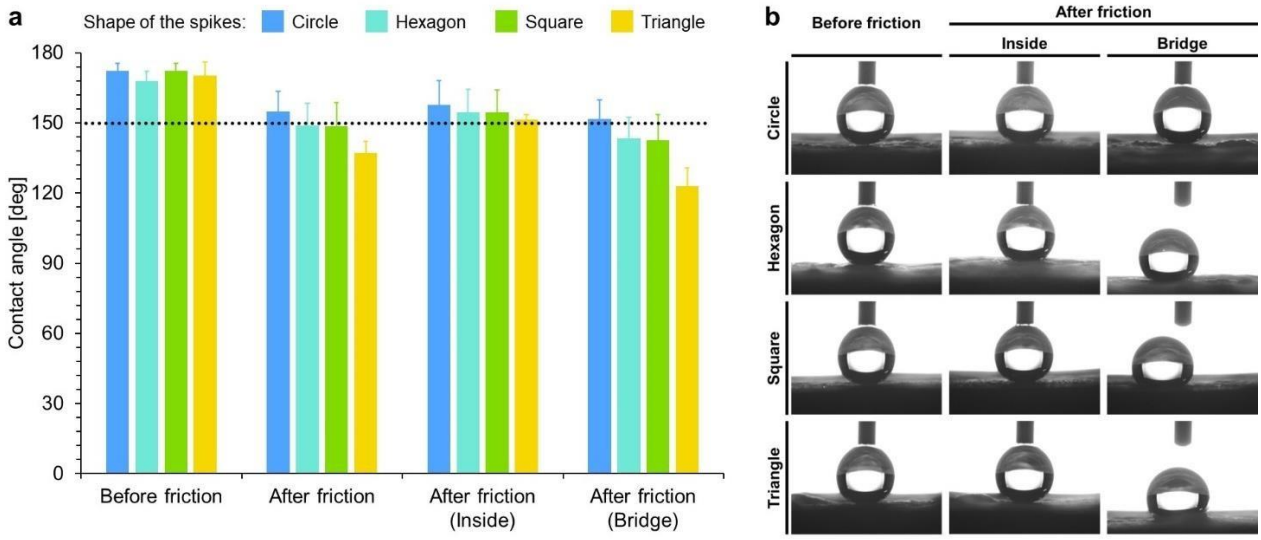

Figure S6. Surface wettability comparison of 3D-printed structures with different spike shapes. (a) Contact angle measurements of 5 µL water droplets on four types of 3D-printed structures, before and after friction durability testing. The friction test consisted of 100 reciprocating cycles under the conditions specified in the experimental section. Results are shown for the hexagon inside, the bridge (outer shell of the hexagon), and the overall average. The black dotted line at 150° marks the superhydrophobicity threshold. (b) Representative images of 5 µL water droplets during contact angle measurements before and after the friction durability test, illustrating the droplet behavior on the hexagon interior and bridge structures for all four spike shape configurations.

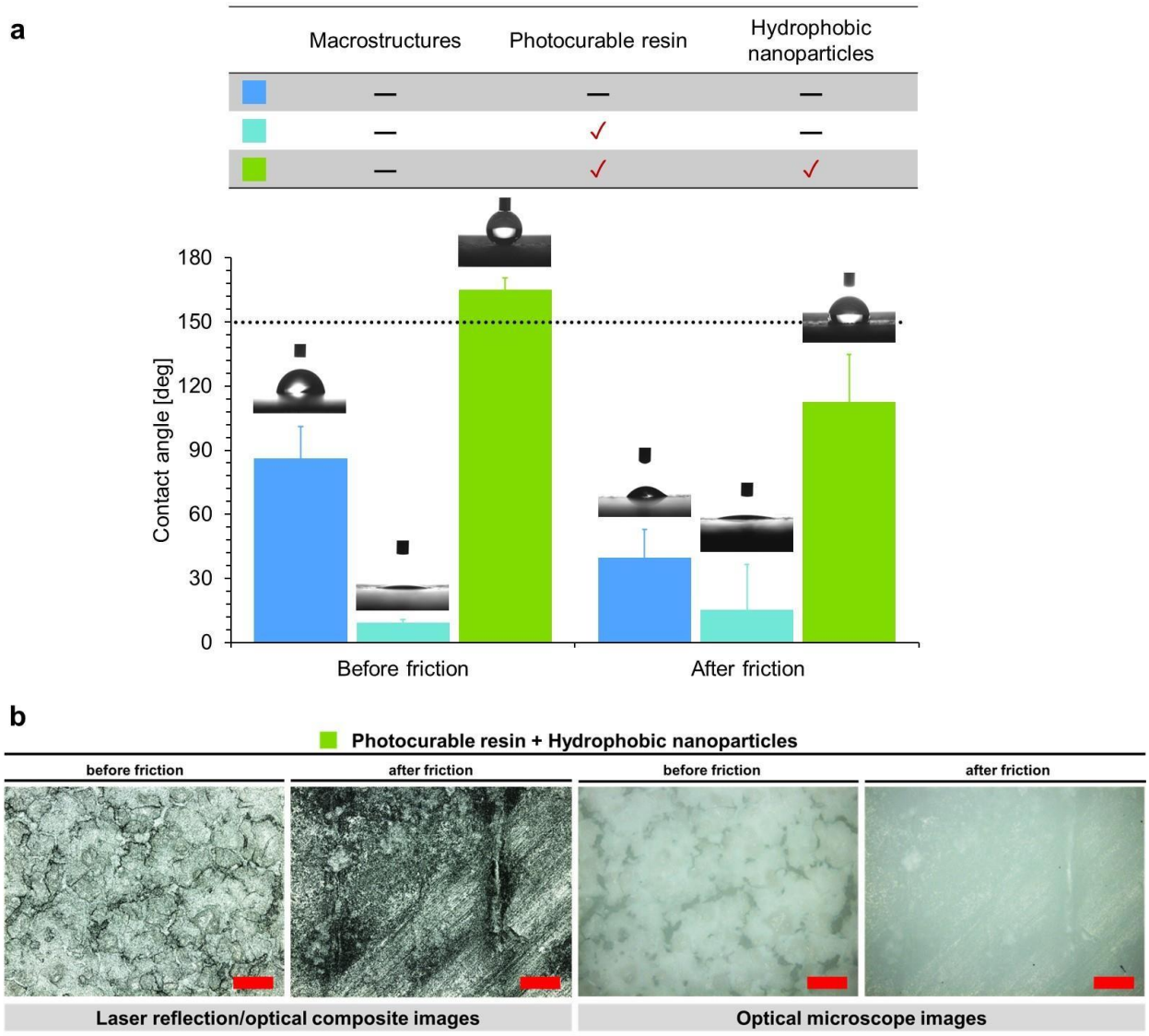

Figure S7. Surface wettability changes of various coatings without honeycomb-structured barriers. (a) Contact angle measurements of 5 µL water droplets before and after friction durability testing on different surface treatments. Blue bars: Uncoated PLA surface; Light blue bars: PLA surface coated with photocurable resin only; Green bars: PLA surface with a superhydrophobic coating (photocurable resin and hydrophobic nanoparticles). The friction test consisted of 100 reciprocating cycles under the conditions specified in the experimental section. The results represent the overall average wettability. The inset images show representative 5 µL water droplets during contact angle measurements before and after the friction durability test for each condition. The black dotted line at 150° marks the superhydrophobicity threshold. (b) Representative surface morphology changes before and after friction durability testing for the PLA surface with a superhydrophobic coating (photocurable resin and hydrophobic nanoparticles) in the absence of a barrier macrostructure. The images were obtained using 3D scanning laser microscopy. All red scale bars represent 200 µm.

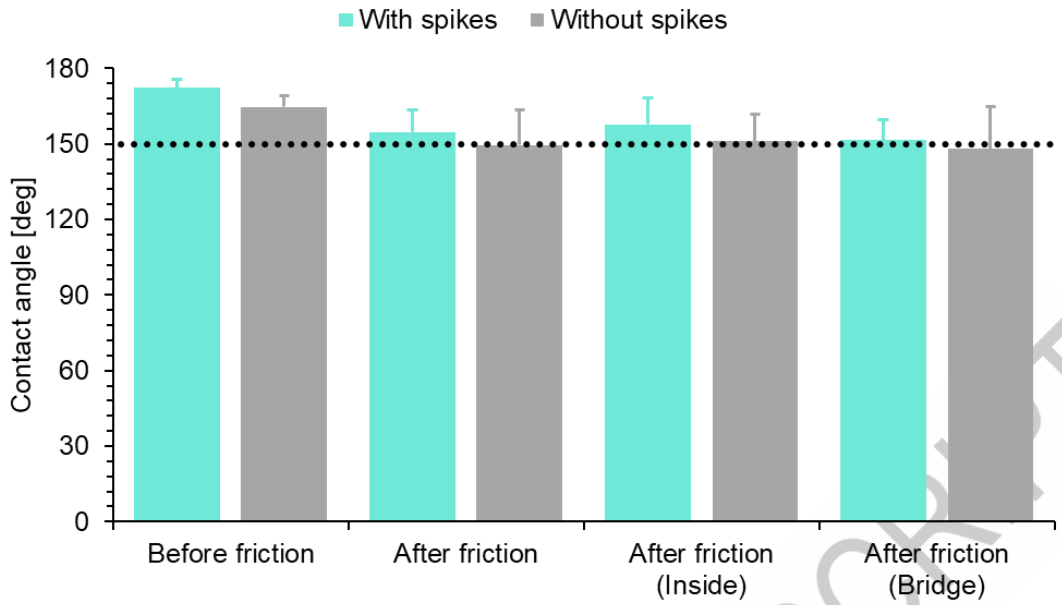

Figure S8. Comparison of friction durability with and without spikes. The effect of the presence of spikes within the hexagonal macrostructure on the superhydrophobicity before and after the friction test was evaluated. The contact angle of a 5 µL water droplet was measured on each surface before and after 100 reciprocating friction cycles under the conditions specified in the experimental section. The black dotted line at 150° indicates the superhydrophobicity threshold.

Applicability of 3D-Printed Superhydrophobic Structures.

This section highlights the practical applicability of the developed superhydrophobic structures. A primary advantage of 3D printing is its ability to produce complex, free-form geometries. In addition, the PLA filament used in this study is available in different colors and transparencies, increasing its versatility for various applications.

Figure S9a shows a model house fabricated using 3D printing techniques. The walls were printed with white PLA filament, while transparent PLA filament was used for the windows. The roof, inspired by the beehive structure validated in this study, was designed with a honeycomb pattern and subsequently treated with the developed superhydrophobic coating. This demonstration effectively illustrates the feasibility of integrating superhydrophobic properties into architectural designs.

In addition, a transparent superhydrophobic structure was fabricated using a transparent PLA filament (Figure S9b). The photocurable resin used in the experiment was also transparent, allowing the creation of a superhydrophobic surface with sufficient optical clarity to allow visualization of a

logo positioned behind it. This example illustrates the potential for preserving transparency while imparting superhydrophobic functionality.

These application demonstrations highlight the versatility and potential utility of the superhydrophobic structures developed. The ability to integrate these properties into 3D-printed objects suggests promising applications across multiple industries. For example, in architecture, superhydrophobic coatings could be applied to building facades or roofing materials to enhance water repellency and self-cleaning properties. In the automotive sector, these coatings could improve visibility by preventing water from collecting on vehicle surfaces such as windshields and mirrors. Moreover, the demonstration of transparent superhydrophobic structures suggests potential applications in optical devices, including lenses, displays, and solar panels, where maintaining optical transparency while ensuring water repellency is critical. The fusion of 3D printing with superhydrophobic surface treatments represents a powerful strategy for developing customized functional materials. This approach not only facilitates the fabrication of complex geometries but also enables the direct integration of superhydrophobicity into a wide range of products and materials, potentially driving innovation in many fields.

Figure S9. Practical applications of 3D-printed superhydrophobic surfaces. (a) Model house (5 cm × 5 cm × 9 cm) featuring a 3D-printed superhydrophobic roof. The roof incorporates a durable superhydrophobic structure inspired by the honeycomb design developed in the study. The image demonstrates the potential for integrating superhydrophobic properties into architectural elements. (b) Transparent superhydrophobic structure. The structure shows the combination of transparency and superhydrophobicity, achieved by using transparent PLA filament and transparent photocurable resin. The image illustrates the visibility through the structure while maintaining superhydrophobic properties.

Table S1. Design and measured values of hexagonal shapes of structural surfaces designed by 3D CAD, 3D printed structures, and coated structures before and after friction test

Area of hexagonal shape: 24 mm²	CAD design [mm]	Coated 3D printed structures [mm]	Structures [mm] Before friction	After friction
Bridge width [mm]	0.2	0.33 (SD 0.005)	0.28 (SD 0.048)	0.35 (SD 0.017)
Diameter of spike apex [mm]	0	0.87 (SD 0.041)	0.75 (SD 0.065)	0.73 (SD 0.041)
Bridge length (length of one side of hexagon) [mm]	3.04	2.87 (SD 0.017)	2.94 (SD 0.054)	2.77 (SD 0.050)

Area of hexagonal shape: 40 mm²	CAD design [mm]	Coated 3D printed structures [mm]	Structures [mm] Before friction	After friction
Bridge width [mm]	0.2	0.23 (SD 0.008)	0.24 (SD 0.025)	0.27 (SD 0.045)
Diameter of spike apex [mm]	0	0.52 (SD 0.202)	0.64 (SD 0.073)	0.63 (SD 0.040)
Bridge length (length of one side of hexagon) [mm]	3.92	3.77 (SD 0.065)	3.78 (SD 0.050)	3.71 (SD 0.028)

Area of hexagonal shape: 80 mm²	CAD design [mm]	Coated 3D printed structures [mm]	Structures [mm] Before friction	After friction
Bridge width [mm]	0.2	0.23 (SD 0.008)	0.32 (SD 0.043)	0.24 (SD 0.039)
Diameter of spike apex [mm]	0	0.53 (SD 0.050)	0.54 (SD 0.053)	0.64 (SD 0.012)
Bridge length (length of one side of hexagon) [mm]	5.55	5.37 (SD 0.040)	5.22 (SD 0.052)	5.25 (SD 0.065)

120 mm^2	[mm]	structures [mm]	Before friction	After friction
Bridge width [mm]	0.2	0.32 (SD 0.026)	0.38 (SD 0.070)	0.29 (SD 0.063)
Diameter of spike apex [mm]	0	0.55 (SD 0.024)	0.55 (SD 0.098)	0.73 (SD 0.040)
Bridge length (length of one side of hexagon) [mm]	6.80	6.69 (SD 0.068)	6.42 (SD 0.085)	6.51 (SD 0.052)

Area of hexagonal CAD 3 Coated Structures [mm] **shape:** design D printed

160 mm^2	[mm]	structures [mm]	Before friction	After friction
Bridge width [mm]	0.2	0.32 (SD 0.033)	0.36 (SD 0.005)	0.35 (SD 0.026)
Diameter of spike apex [mm]	0	0.52 (SD 0.022)	0.57 (SD 0.025)	0.68 (SD 0.057)
Bridge length (length of one side of hexagon) [mm]	7.85	7.77 (SD 0.114)	7.66 (SD 0.172)	7.58 (SD 0.074)

Area of hexagonal CAD Coated Structures [mm] **shape:** design 3D printed

200 mm^2	[mm]	structures [mm]	Before friction	After friction
Bridge width [mm]	0.2	0.32 (SD 0.017)	0.35 (SD 0.014)	0.24 (SD 0.031)
Diameter of spike apex [mm]	0	0.46 (SD 0.005)	0.51 (SD 0.024)	0.56 (SD 0.038)
Bridge length (length of one side of hexagon) [mm]	8.77	8.55 (SD 0.036)	8.48 (SD 0.064)	8.55 (SD 0.160)

Area of hexagonal CAD D printed Coated Structures [mm] **shape:** design 3

Table S2. Comprehensive comparison of superhydrophobic surfaces fabricated using various 3D printing methods and materials, with a focus on their durability

3D	**Contact angle**	**Contact**

Year	Printing Method	Materials	Shape and size	Durability Evaluation	angle after durability test	angle after durability test	Ref
2017	Direct Ink Writing	PDMS + silica nanoparticles	Mesh membrane. thickness of ~0.8 mm.	bending, stretching	150°>	150°>	S1
2018	FDM	PLA + PS nanospheres	Mesh membranes. microscale papillae (diameters from 5 to 9 μm), PS nanospheres (with average diameters of 100 nm)	1000# mesh abrasive paper under a normal pressure of 5 N (provided by standard weights of 500 mg)	151.7°	143° after 10 rounds of abrasion	S2
2020	DLP	DPGDA + TMPTA + hydrophobic fumed silica particles	Pillars. side-lengths (x): 70, 85, 100, 115, 130 μm. height (z): 100-600 μm.	Sand paper abrasion with 50 g and 200 g	150°>	No data (A water droplet did not sliding after 200g abrasion.)	S3

2020	SLA	Clear resin (Formlab) + candle soot (CS) or octadecyltrichlorosilane (OTS) coating	66 mm × 20 mm, with square-shaped micropillars of h = 750 μm, D = 410 μm, and S = 400 μm	underwater ultrasonication (0-60 min)	158° (CS), 147° (OTS)	153° (CS), 143° (OTS) for 60 min	S4
2021	DLP	hydrophobic (meth)acrylate monomers and porogen solvents	Various shapes with sub-micrometer porosity for the external and internal surfaces	sandpaper under a pressure of 10 kPa for 10 cm	155°	150°>	31
2021	SLA	Fluorolink MD700 + emulsifying agent (13FOOl)	Membrane with porosity (a median pore size of 30/300 nm)	stretching and twopoint bending tests	161/164°	150°>	S5

2022	Multi Jet	silica nanoparticles and Hexafor 644-D	cylindrical and pyramid shapes. Cylinders: diameter 300 µm, pitch 400 and 500. Pyramids: Side 200 µm, Side by side distance 200 µm, and Height 800 µm.	tape peeling test (50 cycles)	Cylinder: 157° Pyramid: 164°	Cylinder: 152° Pyramid: 153°	S6
2022	SLA	polymeric photocurable resin-type Clear (Formlab) + TiO_2 nanoparticles coatings functionalized by hexadeciltrimethylsiloxane (HTMS)	structure generated by SLA (of around 100µm), SLA 3D printed filaments (of around 10µm), nanoparticles (22 and 100nm)	Repeated contact angle measurements	165°	140°> after 30 cycles	16
2023	selective laser sintering (SLS)	hydrophobic-fumedsilica (HFS)/ polypropyle	Various shapes with 20–70 nm HFS grains and 20–100 µm	sandpaper friction test under a weight of 200 g for	158°	157°	28

		ne grains	PP micrograi ns	1000 times			
			the				
2023	selective laser sintering (SLS)	PP/PTFE composite grains	maximum molding size is 320 (length) × 3 20 (width) × 4 50 (height) mm^3	sandpaper abrasion at 12.5 kPa	158°	154°> after 5000th abrasion	S7
2023	Direct Ink Writing	PDMS + silica nanoparticl es	Mesh structures	Sand paper abrasion with 200 g	155°>	155°>	S8
2024	FDM	PLA + spray coating (PDMS + silica nanoparticl es)	microplate arrays. Width 0.3 mm. Height 3 mm	No test	153-160°	No data	S9

Supporting References

[S1] Lv J, Gong Z, He Z, et al. 3D Printing of a Mechanically Durable Superhydrophobic Porous Membrane for Oil–water Separation. *J. Mater. Chem. A Mater. Energy Sustain.* 2017;5(24):12435–12444. doi:10.1039/C7TA02202F

[S2] Xing R, Huang R, Qi W, et al. Three-Dimensionally Printed Bioinspired Superhydrophobic PLA Membrane for Oil-Water Separation. *AIChE J.* 2018;64(10):3700–3708. doi:10.1002/aic.16347

[S3] Kaur G, Marmur A, Magdassi S. Fabrication of Superhydrophobic 3D Objects by Digital Light Processing. *Additive Manufacturing* 2020;36:101669. doi:10.1016/j.addma.2020.101669

[S4] Aldhaleai A, Tsai PA, Fabrication of Transparent and Microstructured Superhydrophobic Substrates Using Additive Manufacturing. *Langmuir* 2021;37(1):348–356.

doi:10.1021/acs.langmuir.0c02945

[S5] Mayoussi F, Doeven EH, Kick A, et al. Facile Fabrication of Micro-/nanostructured, Superhydrophobic Membranes with Adjustable Porosity by 3D Printing. *J. Mater. Chem. A Mater. Energy Sustain.* 2021;9(37):21379–21386. doi:10.1039/d1ta03352b

[S6] Chand R, Sharma VS, Trehan R, et al. Developing Superhydrophobic Surface Using Multi Jet 3D Printing Durability Analysis. *J. Mater. Eng. Perform.* 2022;32(3):1133–1144. doi:10.1007/s11665-022-07154-z

[S7] Wu Z, Li Y, Shi C, et al. A General Method for Fabricating Polymer-Based Intrinsic Superhydrophobic Objects by a Selective Laser Sintering 3D Printing Strategy. *Composites Part B* 2023;264:110910. doi:10.1016/j.compositesb.2023.110910

[S8] Jiang R, Li Y, Chao S, et al. Direct Write Printing of Ultraviolet-Curable Bulk Superhydrophobic Ink Material. *ACS Appl. Mater. Interfaces* 2023;15(44):52000–52009. doi:10.1021/acsami.3c12375

[S9] Zhao W, Zhan Y, Li W, et al. Application of 3D Printing for Fabrication of Superhydrophobic Surfaces with Reversible Wettability. *RSC Adv.* 2024;14(25):17684–17695. doi:10.1039/d4ra02742f